






## Open Archive Toulouse Archive Ouverte (OATAO)

OATAO is an open access repository that collects the work of Toulouse researchers and makes it freely available over the web where possible

This is an author's version published in: <http://oatao.univ-toulouse.fr/21782>

**Official URL:** <https://doi.org/10.1002/adfm.201200695>

### To cite this version:

Pérez, Carlos R. and Yeon, Sun-Hwa and Segalini, Julie  and Presser, Volker and Taberna, Pierre-Louis  and Simon, Patrice  and Gogotsi, Yury *Structure and Electrochemical Performance of Carbide-Derived Carbon Nanopowders*. (2013) *Advanced Functional Materials*, 23 (8). 1081-1089. ISSN 1616-301X

Any correspondence concerning this service should be sent to the repository administrator: [tech-oatao@listes-diff.inp-toulouse.fr](mailto:tech-oatao@listes-diff.inp-toulouse.fr)

# Structure and Electrochemical Performance of Carbide-Derived Carbon Nanopowders

Carlos R. Pérez, Sun-Hwa Yeon, Julie Ségalini, Volker Presser, Pierre-Louis Taberna, Patrice Simon, and Yury Gogotsi\*

**Microporous carbon materials are widely used in gas storage, sorbents, supercapacitor electrodes, water desalination, and catalyst supports. While these microporous carbons usually have a particle size in the 1–100  $\mu\text{m}$  range, here the synthesis of porous carbide-derived carbon (CDC) with particle diameters around 30 nm by extraction of titanium from nanometer-sized titanium carbide (TiC) powder at temperatures of 200 °C and above is reported. Nanometer-sized CDCs prepared at 200–400 °C show a disordered structure and the presence of CN  $\text{sp}^1$  bonds. Above 400 °C, the CN bond disappears with the structure transition to disordered carbon similar to that observed after synthesis from carbide micropowders. Compared to CDCs produced from micrometer-sized TiC, nano-CDC has a broader pore size distribution due to interparticle porosity and a large contribution from the surface layers. The material shows excellent electrochemical performance due to its easily accessible pores and a large specific surface area.**

## 1. Introduction

Porous carbons have been of great interest for applications such as gas storage, chemical energy storage or for use as a catalyst support.<sup>[1–3]</sup> The large surface area generated by chemical or physical activation processes dominates the performance for applications such as sorbents, gas storage media, and porous electrodes in supercapacitors. However, these porous carbon materials are usually characterized by a broad pore size distribution (PSD) in

both the micropore (<2 nm) and the mesopore range (between 2 and 50 nm).<sup>[4–6]</sup> Tighter control of the PSD and matching a narrow distribution with the proper electrolyte has been shown to significantly increase the electrode capacitance,<sup>[7]</sup> especially when the pore diameter approaches the size of the desolvated ions.<sup>[8]</sup>

In carbide-derived carbons (CDCs), the PSD is determined by the structure and type of the precursor and the applied synthesis parameters.<sup>[9,10]</sup> For titanium carbide-derived carbon (TiC-CDC), very narrow PSDs in the 0.5–2.0 nm range have been produced through selective etching of carbides by chlorine treatment.<sup>[11]</sup> The produced material has a large pore volume (up to 1.6  $\text{cm}^3 \text{g}^{-1}$ ) and high specific surface area (up to 2000  $\text{m}^2 \text{g}^{-1}$  without and 3100  $\text{m}^2 \text{g}^{-1}$  with activation),<sup>[12]</sup> resulting in

large adsorption capacity and high double-layer capacitance.<sup>[13]</sup> CDC formation has been studied for a large variety of precursors, such as ceramic plates,<sup>[14]</sup> fibers,<sup>[15,16]</sup> and micrometer- or nanometer-sized powders and for most carbides, the carbide-to-carbon transformation can be considered to be a conformal process since the size and shape of the carbide precursor is largely maintained.<sup>[17]</sup> This allows synthesis of porous carbon particles of any size, as metal carbides are commercially available with particles ranging from 20 nm to hundreds of micrometers. In contrast, it is difficult to produce activated carbons with such a small particle size.

Micrometer-sized binary carbide powders of, for example, TiC, SiC, ZrC, and  $\text{Mo}_2\text{C}$ , have been extensively studied as CDC precursors for use as supercapacitor electrodes because of the fine control over the pore size by varying the chlorine etching temperature in the range between 200 and 1200 °C.<sup>[10,18–20]</sup> TiC-CDC has attracted significant interest because of its high specific capacitance in various electrolytes.<sup>[21–24]</sup> However, until now, CDC synthesis at temperatures below 400 °C has received little attention,<sup>[11]</sup> mainly because of kinetic limitations that become obvious when micrometer and larger particles or bulk ceramics are used. Low-temperature CDC formation offers not only a low-energy route for the production of porous carbon but will give new insights into the onset of carbide-to-carbon transformation with possibly highly reactive and strongly disordered carbons compared to ordered, graphitic carbon at higher synthesis temperatures. Nanometer-sized precursor particles have shorter diffusion lengths and higher reactivity due to

C. R. Pérez, Dr. V. Presser,<sup>[†]</sup> Prof. Y. Gogotsi  
Department of Materials Science and Engineering &  
A.J. Drexel Nanotechnology Institute  
Drexel University  
Philadelphia, PA 19104, USA  
E-mail: gogotsi@drexel.edu

Dr. S.-H. Yeon  
Distributed Power Generation and Energy Storage Group  
Korea Institute of Energy Research  
Daejeon, 305-343, South Korea

Dr. J. Ségalini, Dr. P.-Louis Taberna, Prof. P. Simon  
Universite Paul Sabatier  
CIRIMAT UMR-CNRS 5085  
118 route de Narbonne 31062 Toulouse Cedex 9–France  
Réseau National sur le Stockage Electrochimique de l’Energie  
FR CNRS n 3459

[†] Present Address: INM-Leibniz Institute for New Materials, Energy Materials Group, Campus D2 2, D-66123 Saarbrücken, Germany

DOI: 10.1002/adfm.201200695

significantly increased surface area, and have previously shown that CDC synthesis temperatures as low as 200 °C are possible.<sup>[25]</sup>

High specific capacitance and capacity retention have been previously reported for silicon carbide-derived carbon nanoparticles,<sup>[17,26]</sup> but their synthesis required temperatures higher than ~600 °C. As previously reported for mesoporous carbon nanospheres,<sup>[27]</sup> mesoporous CDCs with hierarchical pore structure,<sup>[27–29]</sup> CDC thin films<sup>[30]</sup> and exohedral carbon nanoparticles,<sup>[31]</sup> the shorter diffusion path length for electrolyte ions results in improved power handling ability for supercapacitor applications. Initial studies on SiC-CDC nanoparticles have documented the improved power handling ability and high specific capacitance compared to micrometer-sized SiC-CDC,<sup>[29]</sup> however, until now, there has not been a systematic study that investigates the structure of such nanometer-sized CDCs. Nanometer-sized CDC would also be advantageous for preparation of stable colloid suspensions, such as inks, enabling printing techniques for the manufacture of supercapacitor or fuel cell electrodes.<sup>[32]</sup>

Here, we report on the synthesis of nano-TiC-CDC (referred to as nano-CDC) with mean particle sizes around 20–40 nm in the temperature range between 200 and 1200 °C, investigate the electrochemical behavior as a function of CDC structure, PSD and specific surface area (SSA), and compare it to micrometer-sized TiC-CDC (referred to as micro-CDC).

## 2. Results and Discussion

### 2.1. Structure of Nano-CDC

All studied samples at all temperatures were almost fully converted into nano-CDC after chlorine treatment as seen from the XRD pattern shown in **Figure 1a**. Samples synthesized at temperatures lower than 600 °C were treated longer, that is, 5 h of chlorine treatment instead of 3 h, to ensure the completion of

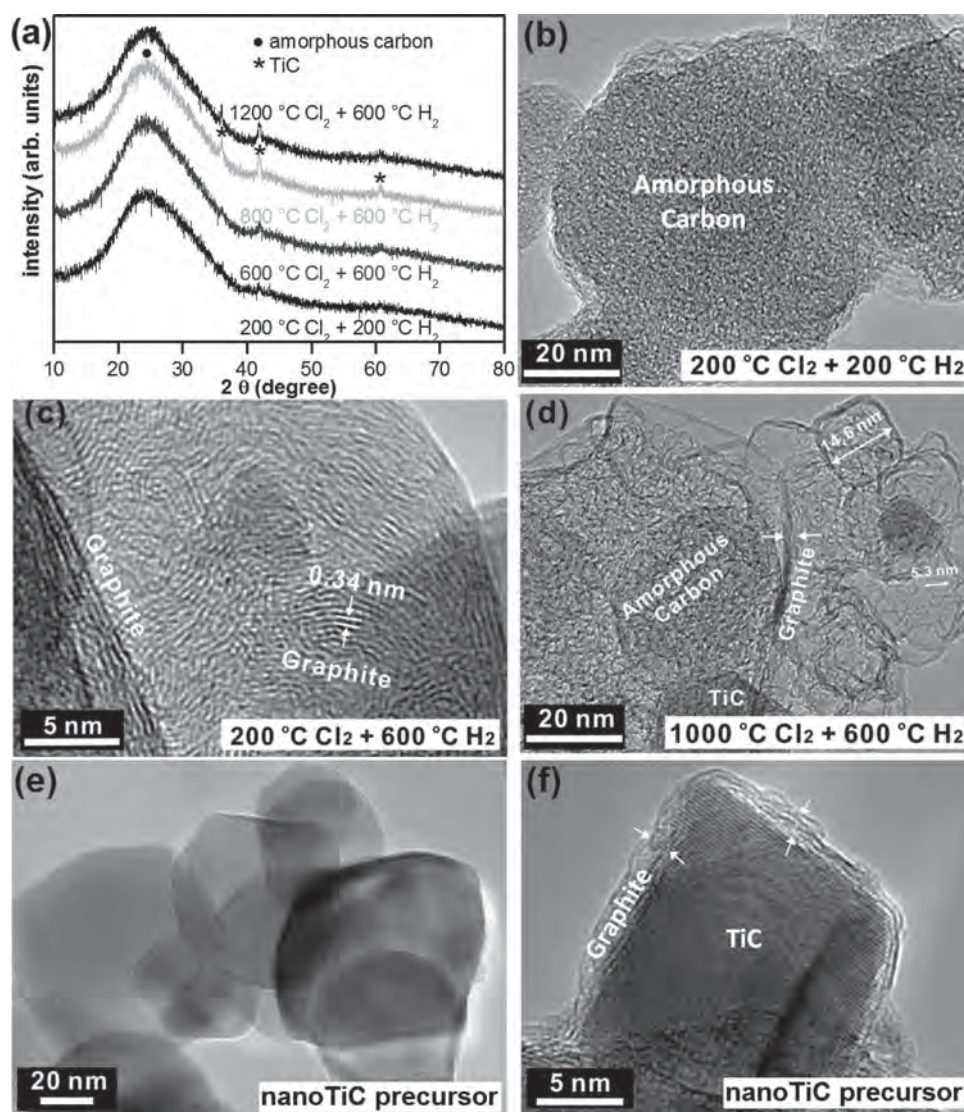


**Figure 1.** a) XRD patterns of nano-TiC-CDCs synthesized at 200–1200 °C (PDF #32-1383). TEM images of nano-TiC-CDC synthesized and H<sub>2</sub>-annealed at indicated temperatures (b–d) and nano-TiC precursor (e,f).

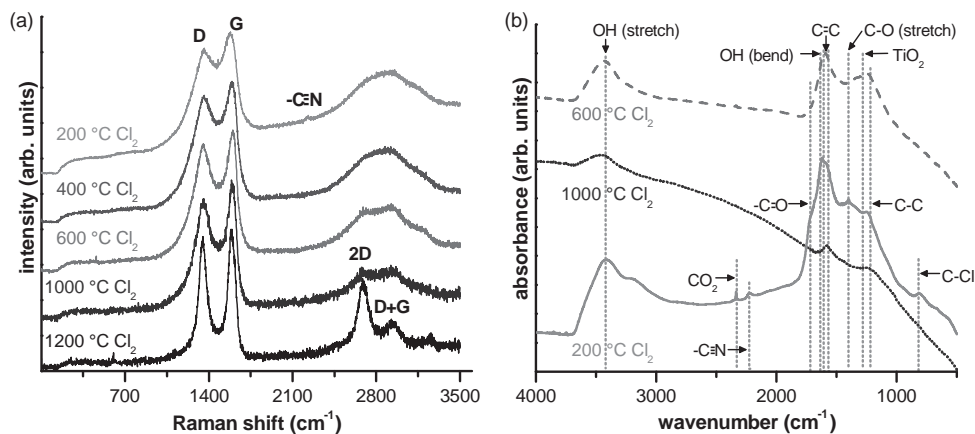


**Figure 2.** a) Raman and b) FTIR spectra of nano-CDCs synthesized at 200–1200 °C with subsequent hydrogen annealing. Nano-CDCs synthesized at 200 and 400 °C were annealed the same temperatures. All other samples were annealed at 600 °C. The Raman spectra were normalized to the intensity of the G-band at 1582  $\text{cm}^{-1}$  and shifted along the Y-axis for clarity.

the reaction. It is important to note that no produced CDCs from low temperature chlorine treatment show significant amounts of residual TiC precursor, while at higher temperatures higher TiC contents can be identified, but never more than 5 wt%. The Bragg reflection at around  $2\theta$ , corresponding to the diffuse scattering from disordered amorphous carbon, shows a large full width at half maximum (FWHM) that indicates the amorphous nature of nano-CDC.

Figure 1b–d shows high-resolution TEM images of the carbide precursor and nano-CDC synthesized at 200 and 1000 °C, respectively. As-received TiC nanoparticles are uniform idiomorphic cubes which are often surrounded by a few layers of graphitic carbon (Figure 1e,f). Chlorine treatment at 200 °C and subsequent  $\text{H}_2$  annealing at the same temperature results in completely amorphous carbon (Figure 1b) with no evidence of graphite fringes. Carbon ordering and the formation of graphitic planes starts at temperatures higher than 600 °C as shown in Figure 1c, where nano-CDC synthesized at 200 °C was subject to high-temperature  $\text{H}_2$  annealing at 600 °C. This illustrates how strongly the resulting CDC nanostructure depends on the synthesis temperature. Amorphous carbon coexists with graphitic inclusions at higher temperatures, as seen from Figure 1d. Noticeable graphitization occurs at higher reaction temperatures as seen from Figure 1d, where graphitic carbon layer, amorphous carbon, and unreacted TiC are present. At lower temperatures, incomplete transformation may be a result of insufficient synthesis time; at higher temperatures, the mechanism is different. The incomplete reaction at higher temperatures (1000 °C) shown in Figure 1d and in the XRD diffractograms in Figure 1a can be correlated with the graphitic shells covering the TiC nanoparticles and preventing complete carbide-to-carbon transformation. This diffusion barrier is more effective at higher temperatures, where graphitic carbon forms.

As typical for disordered carbon, nano-CDC (Figure 2a) exhibits a broad disorder-induced D-mode ( $\approx 1356 \text{ cm}^{-1}$ ) and in-plane vibrational G-mode ( $\approx 1579 \text{ cm}^{-1}$ ). This is in agreement with previous studies on CDC powders and TiC-CDC in particular.<sup>[33]</sup> The carbons show a higher degree of ordering with increasing synthesis temperature and the most ordered graphitic material is observed at 1200 °C as evidenced by narrow D- and

G-peaks with the 2D and D+G modes appear at  $\approx 2706 \text{ cm}^{-1}$  and  $\approx 2950 \text{ cm}^{-1}$ , respectively. Only in the case of 200 °C synthesis (Figure 2a) additional Raman-active modes appear at  $\approx 2220 \text{ cm}^{-1}$  and at  $1150 \text{ cm}^{-1}$ . These modes were not observed at higher synthesis temperatures and have never been described for any CDC material in the reviewed literature.<sup>[10,11,34]</sup> These signals correspond to the stretching mode of sp-bonded carbon nitrile  $\text{C}\equiv\text{N}$ <sup>[35,36]</sup> and a C-N mode, respectively.<sup>[37]</sup> The FTIR spectrum (Figure 2b) presents additional evidence of  $\text{C}\equiv\text{N}$  bonds as the  $2227 \text{ cm}^{-1}$  band in nano-CDC synthesized at 200 °C.

The high reactivity of CDC obtained by chlorine treatment of nano-TiC at 200 °C can be seen as the reason for CN bond formation. In order to investigate the reactivity of nano-CDC, thermal analysis was carried out in air. The onset of CDC oxidation obtained from chlorine treatment at 200 °C (Figure 3a) was observed at 150 °C which is significantly lower than for any other CDC reported so far and indicates its high reactivity of this highly disordered carbon. With increased synthesis temperature, nano-CDCs exhibit increased thermal stability. When comparing the mass loss of CDC prepared at 1000 and 1200 °C to nano-CDC from chlorine treatment at 200 or 400 °C, oxidation starts at significantly higher temperatures ( $>350 \text{ °C}$ ). Comparing the maximum in the oxidation rate as the derivative of the TG curve (Figure 3b), we see that the maximum rate shifts linearly from 410 °C for nano-TiC synthesized at 200 to 548 °C for CDC produced at 1000 °C. CDCs from micrometer-sized precursors begin to exhibit significantly lower reactivities when compared to nano-CDCs synthesized at similar temperatures. The high ash content ( $\approx 20\%$ ) of the micro-CDC sample synthesized at 200 °C is caused by the low mobility of  $\text{Cl}_2$  and chloride below thermodynamic equilibrium condition, which prevents complete conversion of micro-CDC.

## 2.2. Porosity of Nano-CDC

Table 1 and Figure 4 provide information on the porosity of nano-CDC. From its PSD (Figure 4a) we find that low-temperature CDC synthesis yields subnanometer pores. By combining  $\text{N}_2$  and  $\text{CO}_2$  gas sorption data, the range between

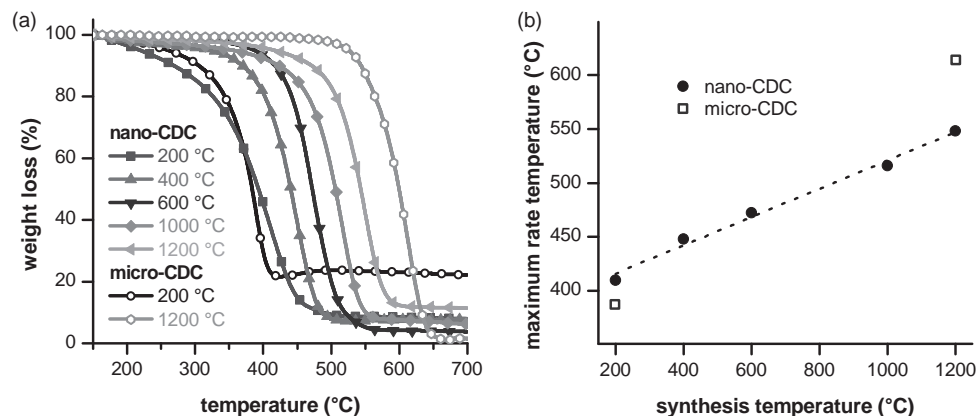


**Figure 3.** a) Thermogravimetric analysis of nano-CDCs synthesized at 200–1200 °C. Experiments were conducted in air at 2 °C min<sup>-1</sup>. Nano-CDCs synthesized at 200 and 400 °C were annealed in H<sub>2</sub> at 200 and 400 °C for 2 h, respectively. All other samples were annealed in H<sub>2</sub> at 600 °C for 2 h. Micro-CDC synthesized at 200 and 1200 °C and annealed at 200 and 600 °C, respectively, are included for reference. b) The temperature of maximum weight loss for the same materials increases linearly with synthesis temperature for each precursor.

0.3 and 30 nm can be probed. The PSD broadens with synthesis temperature as a result of a larger pore volume associated with mesopores; the nitrogen sorption isotherm shows hysteresis typical of cylindrical/slit mesopores. The total pore volume has a maximum value at 1000 °C, and then decreases at 1200 °C due to carbon graphitization (Figure 4d) which is associated with an abrupt increase in the average pore size. It is important to note that annealing of nano-CDC synthesized at the lowest temperature (200 °C) in hydrogen at 600 °C widens the average pore size slightly (+6%) and increases the SSA significantly (+30%). The latter may be the result of more efficient removal of residual chlorine and chlorides trapped in the pores at a higher annealing temperature.

The porosity of nano-CDC is comparable with micro-CDC, but with several important differences: Nano-CDC, due its high reactivity, shows a stronger temperature dependence of porosity than its micrometer-sized counterparts.<sup>[11]</sup> Also, nano-CDC reaches higher maximum SSA values. The PSD SSA has a bell-shape, with a maximum of 2176 m<sup>2</sup> g<sup>-1</sup> at 800 °C, and a

minimum of 730 m<sup>2</sup> g<sup>-1</sup> at 200 °C chlorine treatment temperature. The low BET SSA of the 200 °C sample is due to the pores being too small for N<sub>2</sub> molecules; this is why the DFT SSA (which includes data from CO<sub>2</sub> adsorption) more than doubles the N<sub>2</sub> BET SSA. We note that the total theoretical SSA may be underestimated because of the inaccessibility of such small pores to the gas molecules. However, with the size of the ions used in this study being larger or comparable to the gas-kinetic diameter of nitrogen, we note that the calculated SSA is a good measure for the electrochemically relevant surface area.

### 2.3. Electrochemical Behavior

The specific capacitance of nano-CDC in comparison with micro-CDC is shown in Table 1. Figure 5a shows the cyclic voltammograms measured in H<sub>2</sub>SO<sub>4</sub> electrolyte normalized by scan rate and carbon weight for the four nano-CDC samples synthesized at 200 °C and annealed at 200 °C, and synthesized

**Table 1.** Synthesis conditions, resulting microstructure, and performance in cavity micro-electrodes. Samples in grey rows were also tested for gravimetric capacitance.

Cl <sub>2</sub> temp [°C]	H <sub>2</sub> temp [°C]	Pore volume total [cm <sup>3</sup> g <sup>-1</sup> ]	Pore volume <1.5 nm CO <sub>2</sub> [cm <sup>3</sup> g <sup>-1</sup> ]	S <sub>BET</sub> <sup>a)</sup> N <sub>2</sub> [m <sup>2</sup> g <sup>-1</sup> ]	S <sub>DFT</sub> <sup>b)</sup> N <sub>2</sub> +CO <sub>2</sub> [m <sup>2</sup> g <sup>-1</sup> ]	Mean pore size N <sub>2</sub> +CO <sub>2</sub> [nm]	C <sup>c)</sup> [F g <sup>-1</sup> ]
200	200	0.35	0.14	324	730	0.56	91
200	600	0.48	0.18	434	944	0.58	
400	400	0.66	0.23	740	1348	0.62	
400	600	0.87	0.27	1002	1592	0.69	109
600	600	0.90	0.21	952	1207	0.85	132
800	600	1.66	0.36	1855	2167	0.86	
1000	600	1.73	0.32	1920	2134	0.96	77
1200	600	0.92	0.15	619	687	1.71	
600 <sup>d)</sup>	600	0.83	0.45	1056	1423	0.68	130

<sup>a)</sup>Specific surface area computed using Brunauer-Emmett-Teller method, from nitrogen adsorption isotherm data at -195.79 °C; <sup>b)</sup>Density functional theory specific surface area, combining data from N<sub>2</sub> at -195.79 °C and CO<sub>2</sub> at 0 °C to account for pores too small for N<sub>2</sub>; <sup>c)</sup>Gravimetric capacitance (per electrode) from galvanostatic cycling at 2.5 mA in Swagelok cell; <sup>d)</sup>Micrometer- sized TiC-CDC used as benchmark.

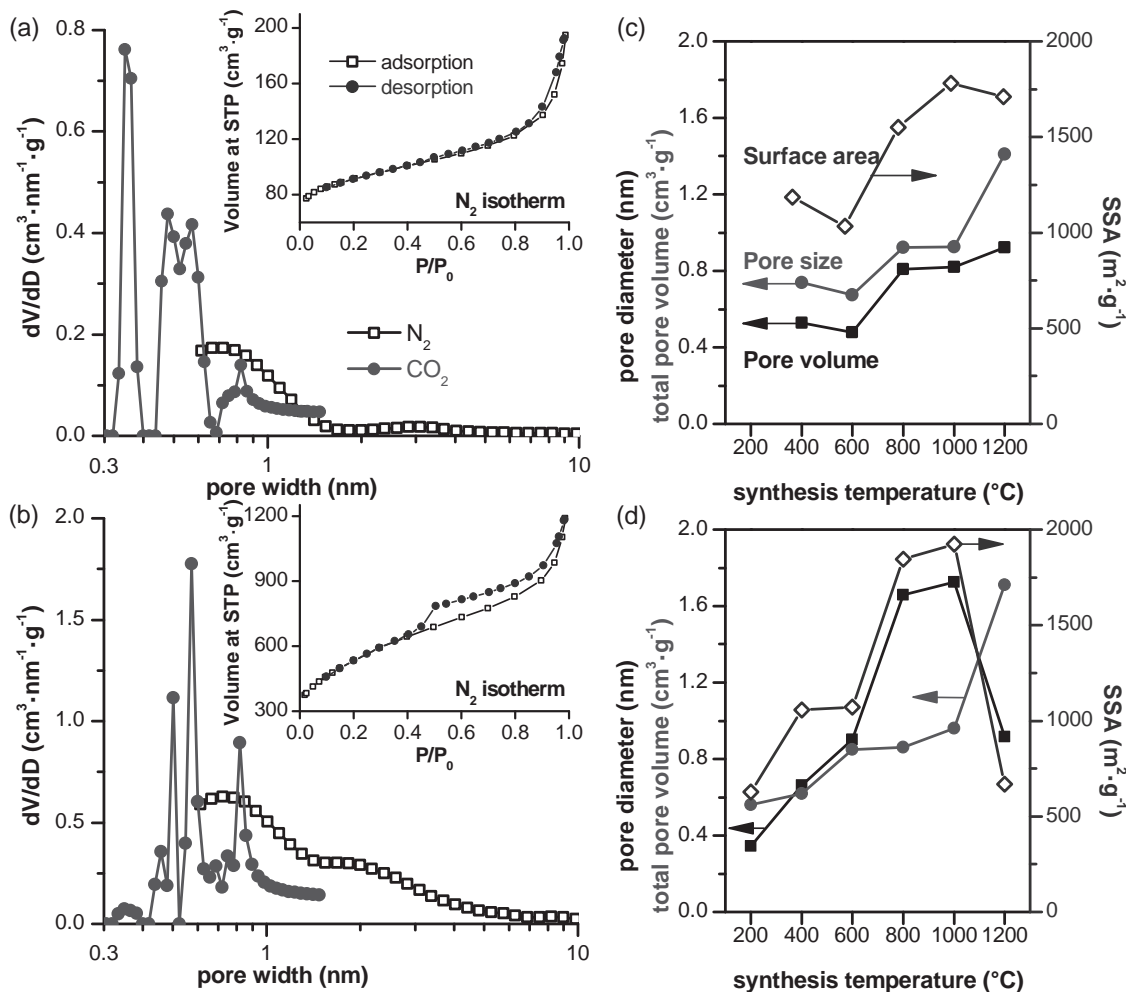


**Figure 4.** Pore size distributions of nano-CDC synthesized at a) 200 and b) 1000 °C and annealed at 200 and 600 °C, respectively. The insets show the nitrogen sorption isotherms while the PSDs are based on N<sub>2</sub> (QSDFIT) and CO<sub>2</sub> (NLDFT) sorption data. c) Average pore size, pore volume, and SSA for CDC from a micrometer-sized TiC precursor synthesized at 400–1200 °C and annealed at 600 °C. d) Average pore size, pore volume and SSA for nano-CDC synthesized at 200–1200 °C and annealed at 600 °C, except for samples synthesized at 200 and 400 °C, which were annealed at the same temperature.

at 400, 600 and 1000 °C, all three annealed at 600 °C. In these 3-electrode experiments, the nano-CDC samples were cycled in the positive potential range showing SO<sub>2</sub><sup>-</sup> anions electrosorption. All cyclic voltammograms (CVs) exhibit capacitive behavior (rectangular shape). The electrochemical impedance spectroscopy (EIS) of the Swagelok cells is shown Figure 5b. The high frequency resistance is about 0.3 Ω cm<sup>2</sup>, which is a conventional value for aqueous electrolyte (Inset Figure 5b); as the frequency decreases, a small loop-like shape attributed to contact resistance appears.<sup>[38]</sup> In the low frequency range, the quasi-vertical line parallel to the imaginary axis, observed for all the samples, is typical of a capacitive behavior in agreement with the CVs of Figure 5a. Figure 5c shows the capacitance vs. current density plots obtained from galvanostatic measurements. The capacitance loss is about 25% for all samples which is in good agreement with previous results.<sup>[8]</sup> This result highlights the good charge retention capabilities of nano-CDC samples. The specific capacitance obtained from galvanostatic measurements (at ≈150 mA g<sup>-1</sup>) as a function of pore size (Figure 5c)

shows a maximum for 0.85 nm pore size sample (synthesized and annealed at 600 °C). This value is very close to the optimal pore size found in previous work on micrometer-sized TiC-CDC samples tested in H<sub>2</sub>SO<sub>4</sub> electrolyte<sup>[13]</sup> where the highest capacitance was obtained for a micro-CDC sample with a pore size of 0.8 nm (synthesized at 800 °C and annealed at 600 °C). Nano-CDC thus compares favorably to CDCs from coarser precursor particles, achieving similar capacitive behavior while requiring lower synthesis temperatures. This is as expected from the higher mobility of carbon in CDC nanoparticles, which means that the pore structure of nano-CDC resembles that of a micro-CDC synthesized at a higher temperature.

Additional electrochemical characterizations of nano-CDC materials were carried out with a cavity microelectrode (CME). This technique allows fast qualitative studies of a large range of nano-CDC samples synthesized at different chlorine treatment temperatures (Figures 6,7) and for a comparison with micro-CDC samples. CVs recorded with the CME in H<sub>2</sub>SO<sub>4</sub> on nano-CDC prepared at 400 °C and a micro-CDC synthesized at

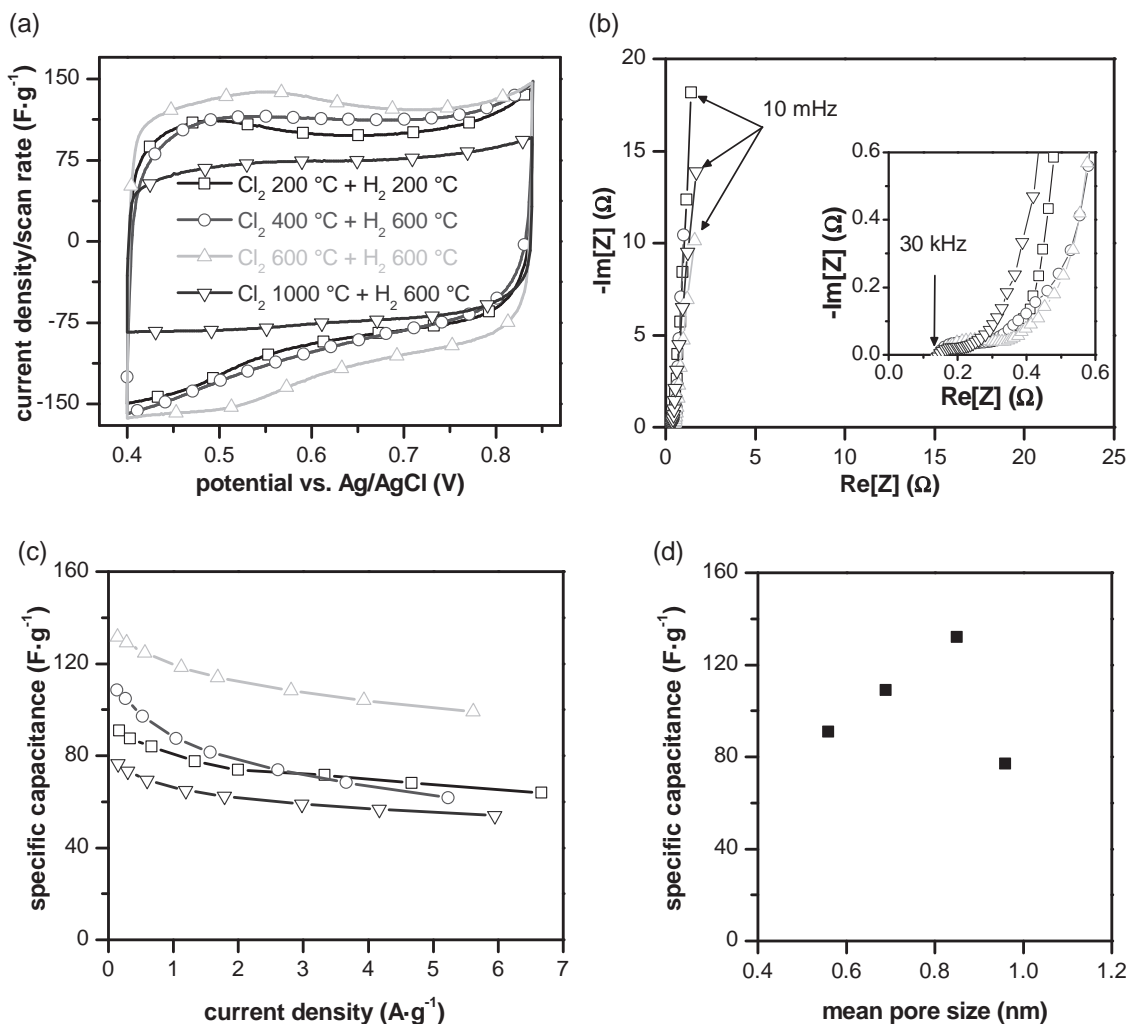


**Figure 5.** a) Cyclic voltammograms of 3-electrode Swagelok cell of nano-CDCs of various pore sizes at  $5 \text{ mV s}^{-1}$  scan rate. b) Electrochemical impedance spectroscopy (EIS) of nano-CDCs of various pore sizes. c) Specific capacitance as a function of current density during galvanostatic cycling of nano-CDCs of various pore sizes in a three-electrode cell. d) Specific capacitance versus pore size of nano-CDC samples.

600 °C are depicted in **Figure 8a**. Both CVs exhibit a similar rectangular shape typical of a capacitive behavior. The capacitance varies with synthesis temperature, and depends on SSA as well as pore size. Microelectrode capacitive behavior similar to those of previously characterized micro-CDC (600 °C) were obtained for nano-CDC synthesized at temperatures as low as 200–400 °C. For lower temperature  $\text{H}_2$  annealing the by-products of the chlorine treatment could potentially remain behind, resulting in lower total accessible pore volumes (Table 1). The contribution of pores to the total capacitance followed the previously reported pattern.<sup>[8]</sup> Capacitance increases as a function of the pore size, up to  $\approx 0.8 \text{ nm}$  (Figure 5d). This size corresponds to that of the solvated sulfate anion  $\text{SO}_4^{2-} \cdot (\text{H}_2\text{O})_{12}$ .<sup>[39]</sup>

Additionally, the relative contribution of capacitive, pseudocapacitive, and faradic charge storage mechanisms was characterized by analyzing CV data taken at various scanning rates.<sup>[40,41]</sup> After plotting steady-state current vs. scanning rate in log-log scale (Figure 8b) the slope of these curves is an indication of the dominant charge storage mechanism, with a value of one representing an ideal supercapacitor, and 0.5 corresponding to

diffusion-controlled processes.<sup>[40]</sup> Capacitive behavior dominates for nano-CDCs synthesized at higher temperatures, but as the microstructure becomes less ordered and more surface groups are present, this is less so. When both synthesis and annealing temperatures are very low (200 °C), the pore size is very small, and so the value dips below 0.6, indicating a diffusion-controlled process, coinciding with the presence of  $\text{C}\equiv\text{N}$  surface groups known to contribute to pseudo-capacitance.<sup>[42,43]</sup> Further functionalization of these nanoparticles' surface might yield a larger contribution from pseudocapacitance and result in an increased charge storage capacity. Additionally, we expect that the performance of low mobility electrolytes such as ionic liquids will be improved by the short ion diffusion lengths the nanoparticles present, as long as pore sizes are properly tailored.<sup>[44]</sup>

### 3. Conclusions

We have produced CDC by chlorine treatment of TiC with the 20–40 nm particle size in the temperature range from 200

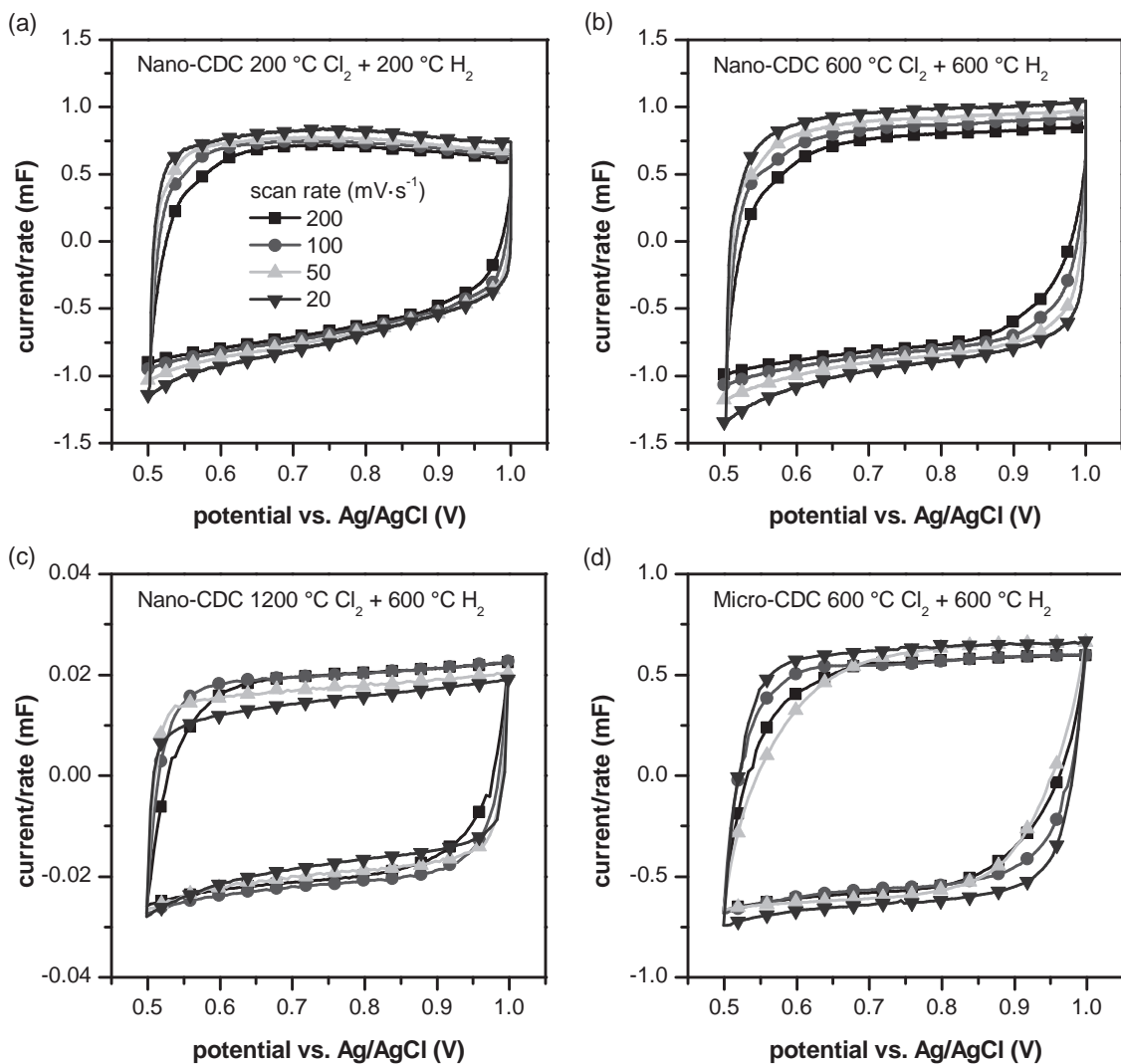


**Figure 6.** Cavity microelectrode voltammograms of micro- and nanometer-sized CDCs synthesized at different temperatures. The current has been normalized by the scanning rate.

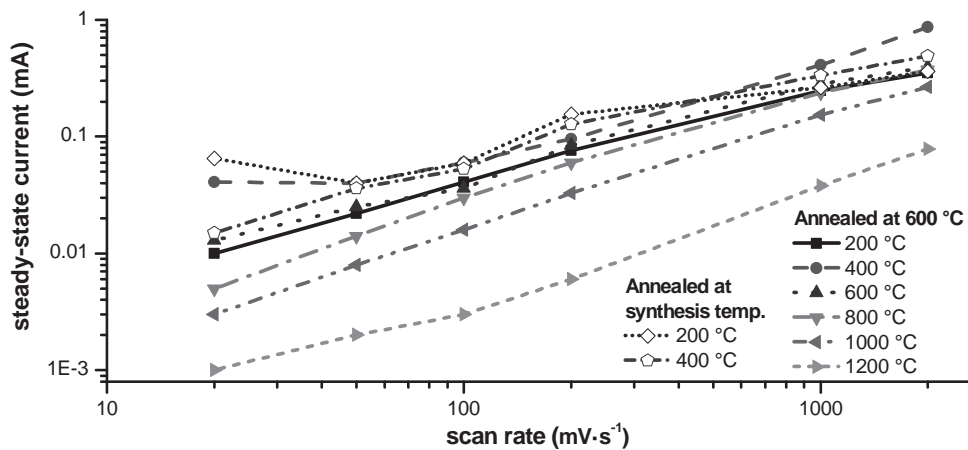


**Figure 7.** Cavity microelectrode steady-state current vs. scanning rate in log-log scale for nano-TiC-CDCs synthesized between 200 and 1200 °C and annealed at 600 °C. Additional curves for CDCs synthesized and annealed at 200 and 400 °C.



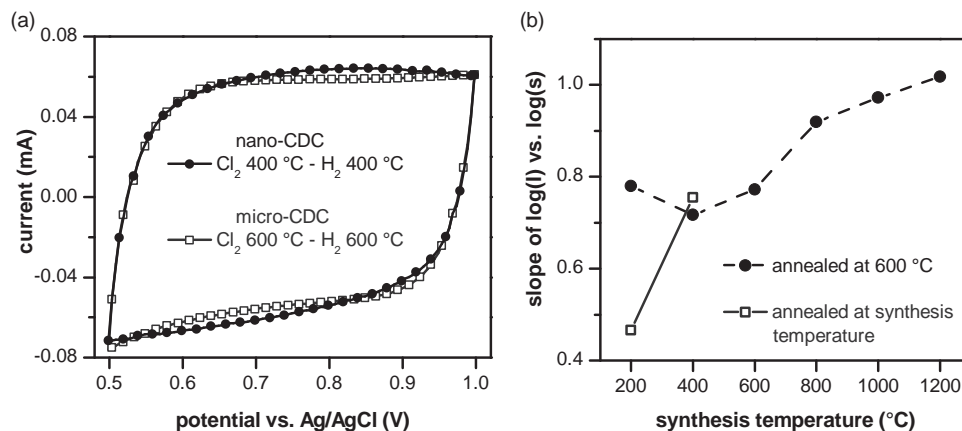


**Figure 8.** a) Cyclic voltammograms recorded in a cavity microelectrode at  $100 \text{ mV s}^{-1}$  with nano-CDC synthesized and annealed at  $400 \text{ }^\circ\text{C}$  and micro-CDC synthesized and annealed at  $600 \text{ }^\circ\text{C}$ . b) Slope of the logarithmic current vs. scanning rate plot, a measure of double-layer vs. diffusion controlled process contribution. Sample synthesized at  $200 \text{ }^\circ\text{C}$  but annealed (in hydrogen) at  $600 \text{ }^\circ\text{C}$  has a higher degree of ordering, while the sample synthesized and annealed at  $200 \text{ }^\circ\text{C}$  better fits the trend. Higher temperature annealing has no effect for the sample synthesized at  $400 \text{ }^\circ\text{C}$ .

to  $1200 \text{ }^\circ\text{C}$ . It is confirmed through  $\text{N}_2$  and  $\text{CO}_2$  gas sorption measurement that nano-CDCs have a broader pore size distribution than CDCs produced from micrometer-size powders. However, while the conversion of nano-TiC to nano-CDC is almost 100% at low temperature ( $200 \text{ }^\circ\text{C}$ ), a small amount of TiC residue remained at high temperatures ( $>600 \text{ }^\circ\text{C}$ ) due to the graphite shells covering some of the nanoparticles. For electrochemical energy storage applications, the capacitance of  $600 \text{ }^\circ\text{C}$  nano-CDC (annealed at  $600 \text{ }^\circ\text{C}$  of  $\text{H}_2$ ) reaches the highest value and shows no major Faradic reactions. Better electrochemical performance of the CDC produced at  $600 \text{ }^\circ\text{C}$  can be explained by its high SSA and large pore volume, while maintaining a large fraction of optimum-sized (subnanometer) pores.<sup>[8,45,46]</sup> Small particle size allowed carbon synthesis at temperature as low as  $200 \text{ }^\circ\text{C}$ , where an amorphous carbon structure with a variety of functional groups (C-H, C=O, C-O, and C≡N) was obtained. This C≡N bond was present up to the  $400 \text{ }^\circ\text{C}$  synthesis temperature. The powder produced at  $200 \text{ }^\circ\text{C}$  has very high chemical activity, as shown by its onset of oxidation from the low temperature of  $150 \text{ }^\circ\text{C}$ . We note that the extremely high reactivity and the presence of C≡N bonds are unique aspects of nano-CDC, which are not found for conventional CDC derived from micro-CDCs.

The capacitance of nano-CDC synthesized at  $600 \text{ }^\circ\text{C}$  is similar to that of micrometer-sized powders synthesized at  $800 \text{ }^\circ\text{C}$ , if both are annealed at  $600 \text{ }^\circ\text{C}$ . Power handling improves with the degree of graphitization. These results show that nanoporous CDC nanoparticles have a great potential for supercapacitor applications, by enabling integration with existing materials systems which cannot be exposed to higher synthesis temperatures, and providing similar or better performance than micrometer-sized CDCs.

#### 4. Experimental Section

Nano-CDC powders were produced by chlorine treatment of nano-TiC powder (PlasmaChem Ltd, Germany, purity:  $>99 \text{ wt}\%$ , average particle size:  $10\text{--}30 \text{ nm}$ ; vendor-furnished composition: Si  $<0.01 \text{ wt}\%$ , free C

$<0.75 \text{ wt}\%$ , O  $<1.25 \text{ wt}\%$ ). This precursor was placed in a horizontal tube furnace, purged in an argon flow, and heated to temperatures between  $200$  and  $1200 \text{ }^\circ\text{C}$  under flowing chlorine ( $10\text{--}15 \text{ cm}^3 \text{ min}^{-1}$ ) for  $5 \text{ h}$  (for chlorine treatment below  $600 \text{ }^\circ\text{C}$ ) or  $3 \text{ h}$  (for sample treated in chlorine gas at temperatures  $\geq 600 \text{ }^\circ\text{C}$ ). After flushing residual  $\text{Cl}_2$  with argon for  $30 \text{ min}$ , the samples were then annealed at  $600 \text{ }^\circ\text{C}$  for  $2 \text{ h}$  using  $\text{H}_2$  gas to remove residual chlorine and chlorine containing compounds.<sup>[8,11]</sup> Additionally, separate nano-CDC powders synthesized at  $200\text{--}400 \text{ }^\circ\text{C}$  were annealed under the same temperature, in order to investigate potential structural change during higher temperature annealing, that is,  $600 \text{ }^\circ\text{C}$ . Since sample transfer from the furnace to measurement apparatus involved brief exposure to air, all measurements were preceded by a degassing procedure consisting of at least  $20 \text{ h}$  at  $200 \text{ }^\circ\text{C}$  in  $0.2 \text{ torr}$  vacuum to remove adsorbed water and  $\text{CO}_2$ .

For transmission electron microscopy (TEM), samples were prepared by dispersing the powder in ethanol and placing the solution over a copper grid with a lacey carbon film. The TEM study was performed using the JEOL 2010F microscope at  $200 \text{ kV}$ . Samples were analyzed by micro-Raman spectroscopy (Renishaw 1000) using an Argon ion laser ( $514.5 \text{ nm}$ ) at  $20\times$  magnification ( $\text{NA} = 0.75$ ;  $\approx 2 \text{ } \mu\text{m}$  spot size) and  $<2 \text{ mW}$  laser power on the samples. X-ray diffraction (XRD) analysis was carried out using a Rigaku diffractometer with  $\text{CuK}\alpha$  radiation ( $\lambda = 1.54 \text{ \AA}$ ) operated at  $30 \text{ mA}$  and  $40 \text{ kV}$ . XRD patterns were collected using step scans, with a step size of  $0.01^\circ (2\theta)$  and a count time of  $2 \text{ s}$  per step between  $5$  and  $80^\circ 2\theta$ . DTA-TGA (differential thermal analysis - thermogravimetric analysis) was performed using a SDT 2960 DTA-TGA from TA instruments and a Perkin Elmer TGA 7. A heating rate of  $2 \text{ }^\circ\text{C min}^{-1}$  was chosen for all experiments under dry air condition.

Gas adsorption analysis was performed using Quantachrome Instruments (U.S.A) Quadrasorb with  $\text{N}_2$  adsorbate at  $-196 \text{ }^\circ\text{C}$  and  $\text{CO}_2$  at  $0 \text{ }^\circ\text{C}$ . PSDs and pore volumes were determined using the non-local density functional theory (NLDFT)<sup>[47]</sup> and the quenched solid density functional theory (QSDFT)<sup>[48]</sup> methods provided by Quantachrome's data reduction software for  $\text{N}_2$  and  $\text{CO}_2$  isotherms collected at  $-196 \text{ }^\circ\text{C}$ , and  $0 \text{ }^\circ\text{C}$ , respectively. The BET SSA was determined from  $P/P_0$  range between  $0.05$  and  $0.2$ .

Cyclic voltammetry was performed with cavity microelectrodes<sup>[49]</sup> produced from nano-CDC in  $1 \text{ M H}_2\text{SO}_4$  (aqueous). The micro-cavity electrodes were constructed by first sealing a  $250 \text{ } \mu\text{m}$  diameter platinum wire inside a hollow glass capillary, followed by etching a microcavity using a hot ( $80 \text{ }^\circ\text{C}$ ) aqua regia, as described elsewhere.<sup>[50]</sup> Platinum foil was used as a counter-electrode, with a silver/silver chloride wire as a reference electrode. The voltage window was  $0.5 \text{ V}$  to  $1.0 \text{ V}$  vs. the reference electrode with up to  $100$  cycles recorded at scanning rates between  $20 \text{ mV s}^{-1}$  and  $2 \text{ V s}^{-1}$ . Capacitance was extracted from CV data by fitting the curves to a

series resistance-capacitance (RC) model. The result agreed with the ratio of current to scanning rate for the constant current part of the CV curve.

Gravimetric and volumetric data was obtained from a three-electrode cell (Swagelok), using YP17 activated carbon as over-capacitive counter-electrode, Glass Fiber (250  $\mu\text{m}$ ) (Whatman) as a separator, and Hg/Hg<sub>2</sub>SO<sub>4</sub>/K<sub>2</sub>SO<sub>4</sub> (saturated) reference electrode in 1 M H<sub>2</sub>SO<sub>4</sub> (aqueous). Pellets of nano-CDC with an area of 1.77 cm<sup>2</sup> were prepared, with a carbon weight between 15 and 19 mg and 10% of poly(vinylidene fluoride-co-hexafluoropropene) (PVDF-HFP) binder. They were characterized using cyclic voltammetry (CV, 5 mV s<sup>-1</sup>), galvanostatic cycling (GC, 0.15–7 A g<sup>-1</sup>) and electrochemical impedance spectroscopy (EIS, 100 kHz–10 mHz frequency range, 5 mV amplitude). All electrochemical measurements were performed using a BioLogic VMP3 potentiostat/galvanostat. The potentials measured vs. the Hg/Hg<sub>2</sub>SO<sub>4</sub> electrode by cyclic voltammetry were recalculated vs. the potential of Ag/AgCl electrode for comparison with the cavity microelectrode study. The capacitance was calculated by integration of the current vs. time curve obtained from the galvanostatic measurements.

## Acknowledgements

The authors are grateful to Dr. H.-S. Kim (Samsung Advanced Institute of Technology), Dr. R. K. Dash (Y-Carbon) for experimental help and helpful discussions. XRD and Raman spectroscopy analysis was performed at the Centralized Research Facilities (CRF) at Drexel University and TEM at the LRSM, University of Pennsylvania. The work at Drexel University was supported by the US Department of Energy, Office of Basic Energy Sciences, Division of Materials Sciences and Engineering under award ER46473. V.P. gratefully acknowledges the financial support by the Alexander von Humboldt Foundation. J.S. was supported by Délégation Générale de l'Armement. The authors thank the Partner University Fund (PUF) for funding the collaborative effort between Paul Sabatier and Drexel universities.

Received: March 13, 2012

Revised: May 29, 2012

Published online: July 6, 2012

- [1] C. He, J. Li, J. Cheng, L. Li, P. Li, Z. Hao, Z. P. Xu, *Ind. Eng. Chem. Res.* **2009**, *48*, 6930.
- [2] P. Simon, Y. Gogotsi, *Nat. Mater.* **2008**, *7*, 845.
- [3] R. E. Morris, P. S. Wheatley, *Angew. Chem. Int. Ed.* **2008**, *47*, 4966.
- [4] R. C. Bansal, J.-B. Donnet, F. Stoeckli, *Active Carbon*, Marcel Dekker, New York **1988**.
- [5] C. Liang, Z. Li, S. Dai, *Angew. Chem. Int. Ed.* **2008**, *47*, 3696.
- [6] R. T. Yang, *Frontmatter in Adsorbents: Fundamentals and Applications*, John Wiley & Sons, Inc., Hoboken, NJ **2003**, 13.
- [7] S. Kondrat, C. R. Perez, V. Presser, Y. Gogotsi, A. Kornyshev, *Energy Environ. Sci.* **2012**, *5*, 6474.
- [8] J. Chmiola, G. Yushin, Y. Gogotsi, C. Portet, P. Simon, P. L. Taberna, *Science* **2006**, *313*, 1760.
- [9] Y. Gogotsi, A. Nikitin, H. Ye, W. Zhou, J. E. Fischer, B. Yi, H. C. Foley, M. W. Barsoum, *Nat. Mater.* **2003**, *2*, 591.
- [10] V. Presser, M. Heon, Y. Gogotsi, *Adv. Funct. Mater.* **2011**, *21*, 810.
- [11] R. Dash, J. Chmiola, G. Yushin, Y. Gogotsi, G. Laudisio, J. Singer, J. Fischer, S. Kucheyev, *Carbon* **2006**, *44*, 2489.
- [12] M. Rose, E. Kockrick, I. Senkovska, S. Kaskel, *Carbon* **2010**, *48*, 403.
- [13] J. Chmiola, G. Yushin, R. K. Dash, E. N. Hoffman, J. E. Fischer, M. W. Barsoum, Y. Gogotsi, *Electrochem. Solid-State Lett.* **2005**, *8*, A357.
- [14] S.-H. Yeon, I. Knoke, Y. Gogotsi, J. E. Fischer, *Microporous Mesoporous Mater.* **2010**, *131*, 423.
- [15] Y. G. Gogotsi, M. Yoshimura, M. Kakihana, Y. Kanno, M. Shibuya, *Ceram. Trans.* **1995**, *51*, 243.
- [16] V. Presser, L. Zhang, J. J. Niu, J. McDonough, C. Perez, H. Fong, Y. Gogotsi, *Adv. Energy Mater.* **2011**, *1*, 423.
- [17] C. Portet, G. Yushin, Y. Gogotsi, *J. Electrochem. Soc.* **2008**, *155*, A531.
- [18] S. Osswald, C. Portet, Y. Gogotsi, G. Laudisio, J. P. Singer, J. E. Fischer, V. V. Sokolov, J. A. Kukushkina, A. E. Kravchik, *Solid State Chem.* **2009**, *182*, 1733.
- [19] S.-H. Yeon, S. Osswald, Y. Gogotsi, J. P. Singer, J. M. Simmons, J. E. Fischer, M. A. Lillo-Ródenas, Á. Linares-Solano, *J. Power Sources* **2009**, *191*, 560.
- [20] A. Jänes, T. Thomberg, H. Kurig, E. Lust, *Carbon* **2009**, *47*, 23.
- [21] M. Rose, Y. Korenblit, E. Kockrick, L. Borchardt, M. Oschatz, S. Kaskel, G. Yushin, *Small* **2011**, *7*, 1108.
- [22] H. Kurig, T. Romann, A. Janes, E. Lust, *ECS Trans.* **2010**, *25*, 15.
- [23] A. Jänes, H. Kurig, T. Romann, E. Lust, *Electrochem. Commun.* **2010**, *12*, 535.
- [24] J. A. Fernandez, M. Arulepp, J. Leis, F. Stoeckli, T. A. Centeno, *Electrochem. Acta* **2008**, *53*, 7111.
- [25] V. Presser, J. McDonough, S. H. Yeon, Y. Gogotsi, *Energy Environ. Sci.* **2011**, *4*, 3059.
- [26] B. Rufino, S. Mazerat, M. Couvrat, C. Lorrette, H. Maskrot, R. Paillet, *Carbon* **2011**, *49*, 3073.
- [27] H.-J. Liu, J. Wang, C.-X. Wang, Y.-Y. Xia, *Adv. Energy Mater.* **2011**, *1*, 1101.
- [28] G. Sun, W. Song, X. Liu, W. Qiao, D. Long, L. Ling, *J. Solid State Electrochem.* **2012**, *16*, 1263.
- [29] Y. Korenblit, M. Rose, E. Kockrick, L. Borchardt, A. Kvit, S. Kaskel, G. Yushin, *ACS Nano* **2010**, *4*, 1337.
- [30] J. Chmiola, C. Largeot, P.-L. Taberna, P. Simon, Y. Gogotsi, *Science* **2010**, *328*, 480.
- [31] J. Huang, B. G. Sumpter, V. Meunier, Y. G. Gogotsi, G. Yushin, C. Portet, *J. Mater. Res.* **2010**, *25*, 1525.
- [32] C. R. Barry, N. Z. Lwin, W. Zheng, H. O. Jacobs, *Appl. Phys. Lett.* **2003**, *83*, 5527.
- [33] S. Urbonaite, L. Hålldahl, G. Svensson, *Carbon* **2008**, *46*, 1942.
- [34] R. K. Dash, G. Yushin, Y. Gogotsi, *Microporous Mesoporous Mater.* **2005**, *86*, 50.
- [35] S. E. Rodil, A. C. Ferrari, J. Robertson, W. I. Milne, *J. Appl. Phys.* **2001**, *89*, 5425.
- [36] A. C. Ferrari, S. E. Rodil, J. Robertson, *Phys. Rev. B* **2003**, *67*, 1.
- [37] B. Bouchet-Fabre, G. Lazar, D. Ballutaud, C. Godet, K. Zellama, *Diamond Relat. Mater.* **17**, 700.
- [38] C. Portet, P. L. Taberna, P. Simon, C. Laberty-Robert, *Electrochim. Acta* **2004**, *49*, 905.
- [39] B. Gao, Z.-f. Liu, *J. Chem. Phys.* **2004**, *121*, 8299.
- [40] H. Lindström, S. Södergren, A. Solbrand, H. Rensmo, J. Hjelm, A. Hagfeldt, S.-E. Lindquist, *J. Phys. Chem. B* **1997**, *101*, 7717.
- [41] J. Wang, J. Polleux, J. Lim, B. Dunn, *J. Phys. Chem. C* **2007**, *111*, 14925.
- [42] G. Lota, B. Grzyb, H. Machnikowska, J. Machnikowski, E. Frackowiak, *Chem. Phys. Lett.* **2005**, *404*, 53.
- [43] S. L. Candelaria, B. B. Garcia, D. Liu, G. Cao, *J. Mater. Chem.* **2012**, *22*, 9884.
- [44] A. Kajdos, A. Kvit, F. Jones, J. Jagiello, G. Yushin, *J. Am. Chem. Soc.* **2010**, *132*, 3252.
- [45] J. Chmiola, G. Yushin, R. Dash, Y. Gogotsi, *J. Power Sources* **2006**, *158*, 765.
- [46] G. Feng, P. T. Cummings, *J. Phys. Chem. Lett.* **2011**, *2*, 2859.
- [47] P. I. Ravikovitch, A. V. Neimark, *Colloids Surf., A* **2001**, *187–188*, 11.
- [48] P. I. Ravikovitch, A. V. Neimark, *Langmuir* **2006**, *22*, 11171.
- [49] C. S. Cha, C. M. Li, H. X. Yang, P. F. Liu, *J. Electroanal. Chem.* **1994**, *368*, 47.
- [50] C. Portet, J. Chmiola, Y. Gogotsi, S. Park, K. Lian, *Electrochim. Acta* **2008**, *53*, 7675.